Electronic Supplementary Material (ESI) for Energy & Environmental Science.

Supporting Information

Designing high performance all-small molecule solar cells with non-fullerene acceptors: comprehensive studies on photoexcitation dynamics and charge separation kinetics

Junqing Shi,[1] Anna Isakova,[1] Abasi Abudulimu,[1] Marius van den Berg,[2] Oh Kyu Kwon,[3] Alfred J. Meixner,[2] Soo Young Park,[3,*] Dai Zhang,[2,*] Johannes Gierschner,[1,2,*] Larry Lüer[1,*]

[1] *Madrid Institute for Advanced Studies, IMDEA Nanoscience, Calle Faraday 9, Campus Cantoblanco, 28049 Madrid, Spain.*

[2] *Institute of Physical and Theoretical Chemistry, University of Tubingen, Auf der Morgenstelle 15, 72076 Tubingen, Germany*

[3] *Center for Supramolecular Optoelectronic Materials and WCU Hybrid Materials Program, Department of Materials Science and Engineering, Seoul National University, ENG 445, Seoul 151-744, Korea.*

TABLE OF CONTENTS:

A Optical Spectra and Photophysics in Solution

Absorption and PL spectra of the electron donor p-DTS(FBTTh$_2$)$_2$ and the acceptor NIDCS-MO in chloroform solution are shown as dashed lines in Figure 1b and the corresponding spectroscopic data are given in Table 1. The absorption spectrum (blue dashed line) of p-DTS(FBTTh$_2$)$_2$ in chloroform solution exhibits two distinctive absorbance bands in the visible, i.e. at 3.23 eV (384 nm; A_2) and at 2.14 eV (580 nm; A_1). The PL spectrum (red dashed line) shows a peak maximum at 1.77 eV (699 nm). According to time-dependent density functional calculations (TD-DFT), A_1 is due to the electronic transition from the ground state (S_0) to the first excited singlet state (S_1). This electronic transition is essentially described by an excitation between the highest occupied and lowest unoccupied MOs (HOMO→LUMO). A_2 originates from $S_0 \rightarrow S_6$ (mainly HOMO→LUMO+2; see Table S1). Both absorption and PL spectra are unstructured in chloroform. as recently discussed by A. Köhler and coworkers,[1] this originates mainly from a solvent effect, rather than strongly twisted geometries as observed for other systems; see the discussions in References [S2] and [S3]. In fact, DFT optimization of S_0 shows only twists within the bithiophene moiety, while the main backbone is planar, see Scheme S1.[1] It should be however pointed out, that from DFT there is a clear indication for the coexistence of two rotamers (*syn* and *anti*; see Scheme S1) with only minor energetic difference (0.02 eV) where the absorption of the *anti*-rotamer is red-shifted against *syn* by 0.03 eV (13 nm). This is indeed supported by experimental data; showing different emission spectra depending on the excitation wavelength (see Figure S1). The donor is moderately emissive with a PL quantum yield of $\Phi_F = 0.12$, and a lifetime of $\tau_F = 1.4$ ns, see Table 1.

The absorption spectrum of NIDCS-MO in solution shows a peak at $A_1 = 2.56$ eV (485 nm) that is assigned to $S_0 \rightarrow S_1$ (HOMO→LUMO; see Table S1). In addition, a shoulder at $A_2 = 3.09$ eV (401 nm) is visible, which is only partly of vibronic nature and contains $S_0 \rightarrow S_4$ (see Table S1). The PL spectrum (2.18 eV; 570 nm) shows some vibronic structure, while the absorption is unstructured. As discussed earlier on related compounds,[S2, S4] this phenomenon points to substantially steeper torsional potentials around the (formal) single bonds in S_1 compared to S_0 due to the shortening of the bonds upon electronic excitation. For the same reason, the molecule planarizes in S_1, compared to (the anyway rather planar) S_0 as can be seen in torsions of the vinyl-phenyl bond ($S_{0,1}$: $\theta_i = 7^{\circ}$, 1°; see Scheme S1) and the vinyl-thiophene bond ($S_{0,1}$: $\theta_o = 3^{\circ}$, 1°). It should be stressed in this context, that strong twists between thiophene and naphthalene rings are calculated both in S_0 ($\theta_T = 56^{\circ}$) and S_1 (40°); however, naphthalene exhibits only negligible contributions to the frontier MOs, which constitute $S_0 \rightarrow S_1$ (Figure 1). On the other hand, significant charge-transfer character involving the naphthalene moieties is observed for $S_0 \rightarrow S_4$, see Table S1 and Figure S2.

NIDCS-MO is brightly emissive in solution with $\Phi_F = 0.37$ and $\tau_F = 1.2$ ns (Table 1). It should be stressed at this point that the electron acceptor NIDCS-MO absorbs (and emits) at significantly higher energy as compared to DTS(FBTTh$_2$)$_2$, so that for possible energy transfer in the blended film (*vide infra*), the electron acceptor (donor) acts as energy donor (acceptor).

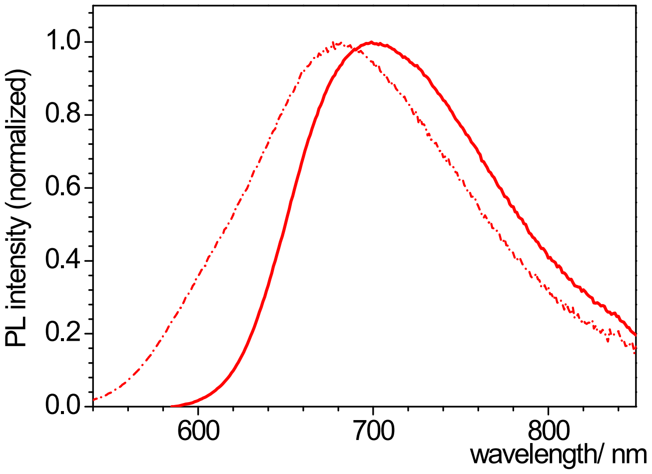

Figure S1: PL spectra of p-DTS(FBTTh$_2$)$_2$ in solution (chloroform); λ_{ex}: 480 nm (dashed line), 580 nm (solid line).

B (TD)DFT Calculations and Results

The geometries of donor and acceptor were optimized at the density functional theory (DFT) level of theory in vacuum under C_2 symmetry restriction; the symmetry restriction keeps the symmetrical situation of the molecules while allowing for complete conformational freedom. For the donor, the optimization was performed for two rotational conformers (*syn*, *anti*) defined by the orientation of closest fluorine with respect to the central sulfur atom (see Scheme S1). Raman spectra were simulated by DFT based on the optimized geometries obtained above; the resulting frequencies were multiplied by 0.97 to correct for the overestimation by the B3LYP functionals. Vertical singlet transitions were calculated using time-dependent (TD)DFT in vacuum; adiabatic singlet transitions were calculated by relaxing the S_1 geometry; the results obtained are listed in Table S1. In all calculations, the alkyl (eg. ethyl and butyl) chains in the central and terminal rings were simply replaced by methyl groups to reduce the computational effort; the B3LYP functional and the 6-311G* basis set were employed as implemented in the Gaussian09 program package.[S5] For the dimer calculation of the donor, we constructed a dimer (Figure S3) by arranging two B3LYPoptimized molecules in the way taken from a published X-ray analysis,[S6] and performed a single point TD-DFT calculation at the CAM-B3LYP level (6-311G* basis set); the calculation results are given in Table S2. Molecular orbitals (MOs) shown in Figure 1 and Figure S2 were visualized with GaussView 5.0.

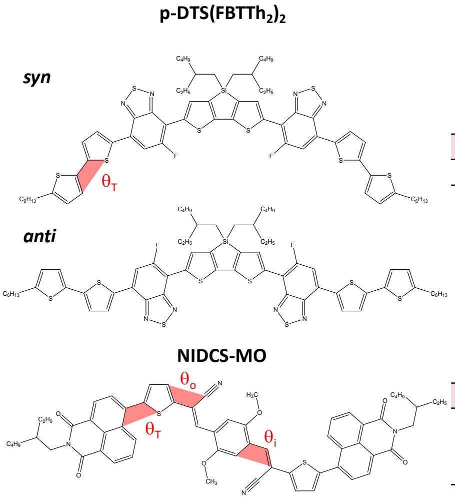

	S_0	S_1
θ_T	20°	8°

	S_0	S_1
θ_i	7°	1°
θ_o	3°	1°
θ_T	56°	40°

Scheme S1: Chemical structures of p-DTS(FBTTh$_2$)$_2$ (*syn*- and *anti*-rotamers) and NIDCS-MO. Relevant torsional angles θ in the ground and first excited state (S_0, S_1) are indicated, calculated by (TD)DFT.

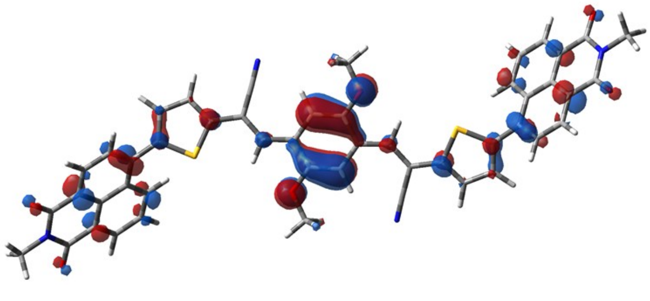

Figure S2: HOMO-2 of NICDCS-MO.

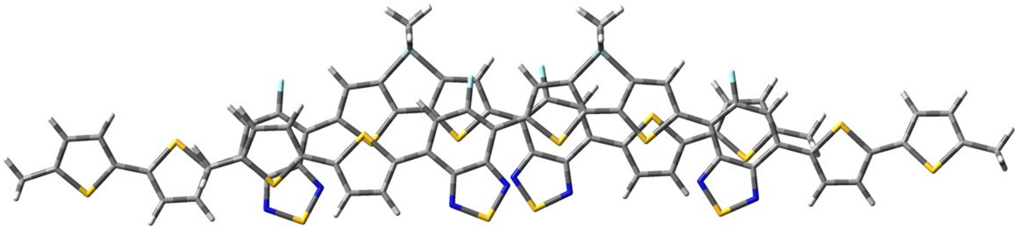

Figure S3: Dimer configuration of p-DTS($FBTTh_2$)$_2$ used for the TD-DFT calculations. The structure of the single molecule was optimized by DFT and the arrangement of two neighboring molecules was adapted according to the reported single crystal X-ray structure (π-stacking distance 3.5 Å).[S6]

Table S1: (TD)DFT calculated excited states of donor (*syn* and *anti* conformers) and acceptor in vacuum (C_2 symmetry): vertical transition energy (E_{vert}), configuration interaction description (CI, values above 5% are listed; H = HOMO, L = LUMO) and corresponding oscillator strength *f*.

molecule	conformer	E_{vert} (eV)	CI (>5%)	*f*
p-DTS(FBTTh$_2$)$_2$	*syn*	S_1(B): 1.67	H→L (97.9)	1.57
		S_2(B): 1.90	H→L+1 (97.5)	0.06
		S_3(A): 2.26	H-1→L (94.6)	0.16
		S_6(B): 2.74	H→L+2 (92.4)	0.95
	anti	S_1(B): 1.64	H→L (98.2)	1.77
		S_2(A): 1.89	H→L+1 (97.0)	0.02
		S_6(B): 2.78	H→L+2 (94.4)	1.12
NIDCS-MO		S_1(A): 2.20	H→L (96.6)	1.71
		S_4(A): 2.82	H-2→L (95.0)	0.33
		S_6(A): 3.23	H-3→L (81.5) H-1→L+1 (10.0)	0.13
		S_8(A): 3.35	H-3→L (11.3) H-2→L+2 (5.7) H-1→L+1 (78.4)	0.15

Table S2: TD-DFT (CAM-B3LYP) calculation on the nearest neighbor dimer arrangement of p-DTS(FBTTh$_2$)$_2$ as shown in Figure S3. Vertical transition energies E_{vert}, configuration interaction description (CI, values above 5% are listed; H = HOMO, L = LUMO) and corresponding oscillator strength *f*. are listed here.

Dimer	E_{vert} (eV)	CI (>5%)	*f*
p-DTS(FBTTh$_2$)$_2$	S_1(A): 1.97	H→L (62.2) H-1→L+1 (13.3)	0.03
	S_2(A): 2.09	H→L+1 (54.8) H-1→L(22.7)	3.15

C Raman Spectroscopy and Imaging

Raman and fluorescence spectra have been collected with a home built confocal setup using a parabolic mirror with a numerical aperture (NA) of 0.998.[S7] As excitation source a 636.3 nm diode laser (Picoquant PDL 800-D) was used and operated in continuous wave mode. Using lambda half wave plates a higher order laser mode is generated to excite the samples with a radially polarized laser beam at ~0.5 µW for both confocal and tip enhanced near-field PL spectra. Gold tips are obtained via electrochemical etching of gold wires (Chempur, 99.99%

purity) in concentrated hydrochloric acid solution with a platinum ring as counter electrode.[S8] These gold tips are then glued to a tuning fork which is brought in the focus to perform shear-force scanning probe microscopy and near-field spectroscopy.[S9, S10, S11, S12] A scanning electron microscope (SEM) image of the gold tip used for this experiment and its corresponding PL spectrum are shown in Figure S5. By monitoring the phase change of the tuning fork using an Ametek 7270 DSP Lock-in amplifier a constant tip sample distance is kept during scanning. PL and Raman spectra are then recorded using a liquid nitrogen cooled charge-coupled device (CCD) chip in combination with a spectrometer (Spectra pro 300i, Acton Research). For PL spectra a 150 grooves/mm grating was used with an integration time of 2 seconds per spectrum except for the PL spectrum of gold tip, which has an integration time of 10 seconds. Raman spectra have been collected using a commercial μ-Raman setup (Jobin-Yvon LabRAM 800 HR UV-vis μ-Raman, Horiba), which has a 532 nm continuous wave laser (Compass 215M-75SL, Coherent) as excitation source. An 1800 grooves/mm grating and 30s integration time per spectrum have been used for collecting the Raman spectra.

We measured Raman spectra and performed confocal/near-field Raman microscopy to visualize the internal composite distribution in BHJ sample and after annealing. We obtained the Raman features of pure donor (1535 cm^{-1}) and acceptor (1565 cm^{-1}), which can be distinguished in the BHJ blend sample (Figure S4). This can be a clue for tracking the spatial distribution in BHJ sample if we get well-resolved Raman mapping images. The peak assignment is currently done through DFT calculations (see below) but not fully evaluated yet; the 1565 cm^{-1} mode is tentatively assigned to the C=O stretch. The calculated Raman spectra agree well with the measured spectra.

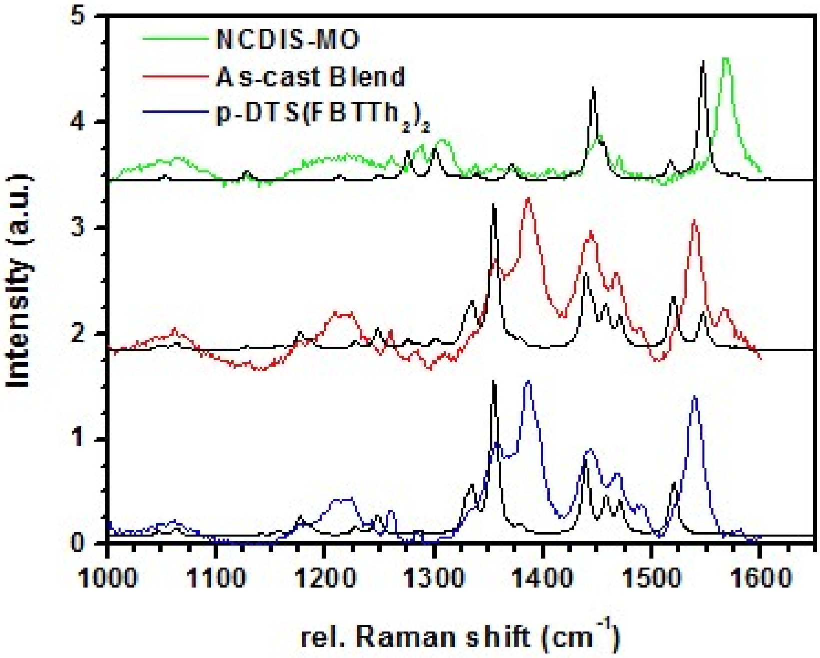

Figure S4: Experimental Raman spectra (in colors) of the as cast films. Excitation: 533 nm. B3LYP-claculated spectra (in black) are listed for comparison.

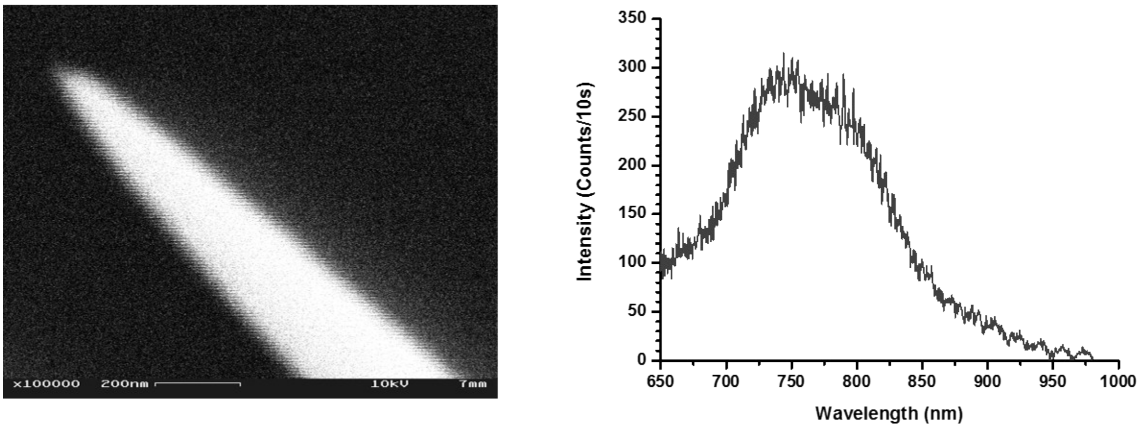

Figure S5: SEM image of the gold tip used, and the gold PL spectrum (10 s integration time).

D Domain Mapping by PL Imaging of the Annealed Blended Film

Variations in the PL spectral shape and intensity are often observed, especially in films with inhomogeneous **D**-**A** distributions.[S9, S10] Conventional optical microscopy in the visible spectral range provides only diffraction-limited resolution, i.e. ca. 200-400 nm. An effective solution to go around the diffraction limit is to use scanning near-field optical microscopy (SNOM). By inserting a sharp gold tip (see Figure S5) in the optical focus it is possible to confine the far-field to a sub-wavelength volume allowing to probe the domain distributions in polymer blends with a nanometer optical resolution down to ca. 10 nm.[S9] This technique is a powerful tool to identify local photophysical properties and morphology changes. We therefore employed confocal and SNOM to study the materials distributions in the as-cast and annealed blend films. Raman fingerprints of **D** and **A** can be readily identified in the as-cast blends, which are tentatively assigned according to the DFT calculations (for details see Figure S4). As PL intensity dominates the optical signals detected, we focus on the PL spectral profile and intensity to obtain the structural information of the blends. PL spectra of **D** and **A** in the as-cast as well as the annealed blends are shown in Figure S6a. In good agreement with Figure 2, PL spectra of the blends are more similar to the donor emission, and annealing barely affects the PL spectral shapes. As seen in Figure S6b, the PL intensity variation is about 15 % for an area of 100 µm x 100 µm . After annealing, SNOM is used to characterize a 1 µm x 1µm area which shows relatively smooth topographic features (Figure S6c, right) and less than 5 % PL intensity variations (Figure S6d). The observations thus confirm the homogeneous distributions of the donor and acceptor components in the blends.

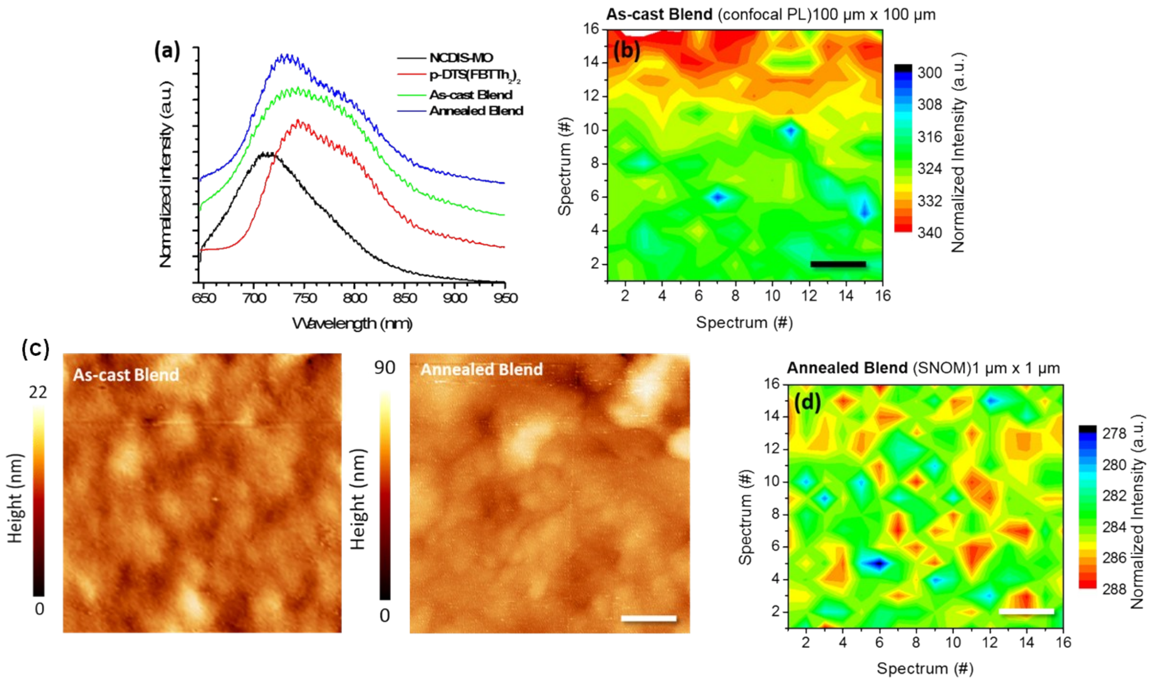

Figure S6: (a) PL spectra from pristine, as-cast blend and annealed blend films. (b) Confocal hyper-spectral PL image of as-cast blend with the black scale bar indicating 20 µm. (c) Topographies of as-cast blend (left, 450 nm x 450 nm) and annealed blend films (right, 1 µm x 1 µm). For more details see also [O K. Kwon, J.-H. Park, D. W. Kim, S. K. Park, S. Y. Park, Adv. Mater. 2015, 27, 1951-1956.] (d) SNOM PL hyperspectral image (16 x 16 spectra) of an annealed blend film that is corresponding to the sample area shown in (c, right).

E Transient Absorption Spectroscopy Analysis

a) Absorption cross-sections

Lambert-Beer's Law relates the optical density (OD) to the concentration of an absorber or molecule or monomer, C_m, given in M=moles/liter:

$$OD = -\,log_{10} T = \varepsilon_m \cdot C_m \cdot d \qquad \text{(S1)}$$

Herein, $T = I_{tr}/I_0$ is the transmission, given by the ratio of transmitted to incident light (I_{tr} and I_0, respectively), d is the film thickness, and ε_m is the molar extinction coefficient, given in units of cm^{-1} M^{-1}. This definition is handy for analytical chemistry. Physicists define Lambert-Beer's law by the natural absorbance A_n:

$$A_n = -\ln T = \sigma_m \cdot c_m \cdot d \qquad \text{(S2)}$$

Herein, the film thickness d is given in cm, the concentration c_m is given in cm^{-3} so that the absorption cross-section σ_m attains the unit cm^2. By using the definition of the base of a logarithm,

$$\log_{10} T = \ln T / \ln 10 \tag{S3}$$

we can insert S1 and S2 into S3 and obtain

$$\varepsilon_m \cdot C_m \cdot d = \sigma_m \cdot c_m \cdot d / \ln 10 \tag{S4}$$

Expressing C_m in units of c_m, that is

$$C_m = c_m \cdot r_{conv} / N_A \tag{S5}$$

N_A=6.022e23 mol^{-1} being Avogadro's constant and r_{conv} = 1000 cm^3/dm^3 the conversion factor between cubic centimeters and liters, we obtain

$$\sigma_m = \varepsilon_m \cdot r_{conv} \cdot \ln 10 / N_A \tag{S6}$$

showing that it is simple to go from σ_m to ε_m and back. Both depend on the irradiated wavelength λ in the same way. The definition of an absorber can be freely chosen; the choice will define the unit for the exciton wavefunction extension in section B. In conjugated polymers, it is convenient to choose a repetition unit as the monomer, while in small molecules, the monomer is obviously the molecule itself. Once a monomer is chosen, its concentration is calculated by

$$c_m = \rho / m_m \tag{S7}$$

where ρ is the specific density of the film (in g cm^{-3}), and m_m is the mass of a monomer in g. Using molecular masses of 1219.89 and 1019.28 g/mol for the donor and acceptor molecule, and a typical density of 1.3 g/cm^3, a film thickness of 95 nm gives the ground state absorption cross-sections as shown in Figure S7.

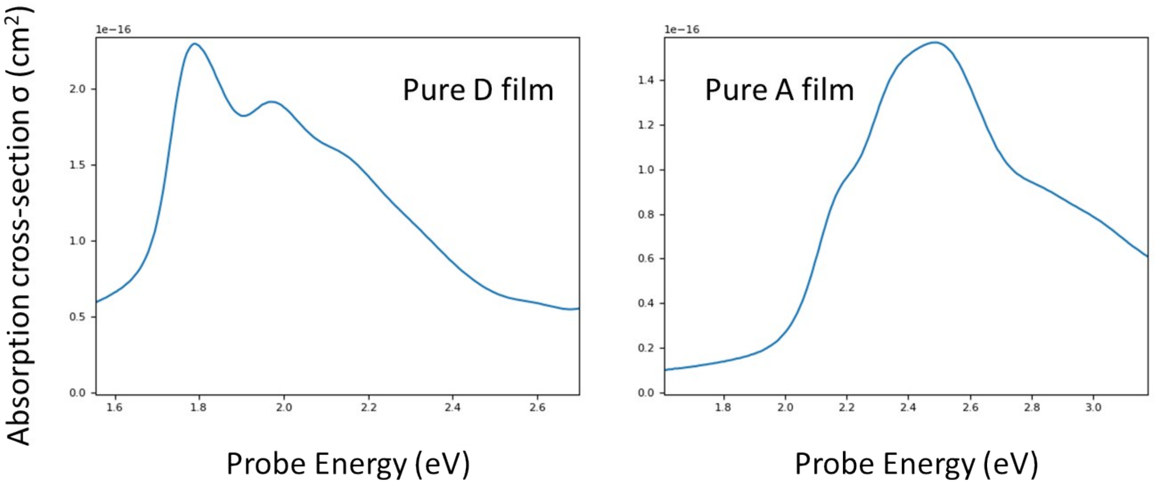

Figure S7: Absolute absorption cross sections of pure donor and acceptor films (left and right panel, respectively).

b) Calculation of excited state delocalization

Quantitative theory of transient photobleach. The theory of transient excitonic optical nonlinearities has been elaborated for two-dimensional excitons[S13] and later applied also to quasi one-dimensional excitons in carbon nanotubes.[S14] The theory relies on the phase space filling model (PSF) requiring that an exciton state cannot be excited twice, because the Pauli exclusion principle must hold. Therefore, the presence of excited states causes a reduction of the ability of the electronic system to absorb further photons at the same wavelength. In transient absorption (TA) spectra, this reduction of the total oscillator strength due to the presence of excited states becomes visible as a transient photobleach (PB). According to the PSF, the relative change of the total oscillator strength f of an absorption band is equal to the relative occupation of available excitations:

$$\frac{\delta f}{f} = - N/N_s \tag{S8}$$

where N is the density of excited states and N_s is the saturation density. The relative change of the total oscillator strength is experimentally accessible by measuring the relative photobleach:

$$\frac{\partial f}{f} = \ - PB_{rel} = \frac{\Delta A}{A_n} \tag{S9}$$

The differential absorption ΔA is given by

$$\Delta A = A_p - A_{np} = \ln\left(T_{np}\right) - \ln\left(T_p\right) = - ln\left(\frac{T_p}{T_{np}}\right) = - ln\left(\frac{T_p - T_{np}}{T_{np}} + 1\right) = - ln\left(\frac{\Delta T}{T} + 1\right) \tag{S10}$$

where A_n is the natural absorbance defined in S2, and the suffices "p" and "np" signify "pump pulse on" and "pump pulse off", respectively. The differential transmission ΔT/T in the right most term in eq. S10 is the quantity usually measured in TA spectroscopy.

Lambert-Beer's law for the differential absorption is given by

$$\Delta A = \sigma_{exc} \cdot c_{exc} \cdot d = \sigma_{exc} \cdot N_{exc} \tag{S11}$$

where σ_{exc} is the cross-section in cm^2 of the ground state bleach caused by one excited state, N_{exc} is the area density of excited states, and c_{exc} is the concentration of excited states, which can be calculated by

$$c_{exc} = N_p \cdot (1 - T)/d \tag{S12}$$

with N_p as the surface density of pump pulse photons (in cm^{-2}) and T is the transmission at the pump wavelength, ignoring reflection and scattering losses. Inserting S11 and S2 into S9, we obtain:

$$\frac{\sigma_{exc}}{\sigma_m} \cdot \frac{c_{exc}}{c_m} = \frac{N}{N_s} \tag{S13}$$

According to the definition, $N = c_{exc}$. The saturation density N_s finally, is related to the size of the excited state L_{exc}, i.e the electron hole correlation length, i.e., the distance at which the probability to find both electron and hole at the same time is 1/e or 1/e^2 of the maximum value for one-dimensional or two-dimensional excited states, respectively. Thus, $N_s = c_m/L_{exc}$ and therefore

$$L_{exc} = \sigma_{exc}/\sigma_m \tag{S14}$$

In the absence of disorder, the result for L_{exc} in S12 should be independent of the chosen detection wavelength as long it is the same for σ_{exc} and σ_m. However, in the presence of disorder, energy relaxation by energy transfer and transient hole burning effects generally cause the spectral shape of the PB band to be markedly different from that of the ground state absorption (A) band. Assuming that disorder acts on the transition energies but not on the transition cross-sections, we can integrate over the respective bands to get a better approximation for L_{exc} for disordered systems:

$$L_{exc}^{disorder} = \frac{\int_{\omega_{min}}^{\omega_{max}} \sigma_{exc}(\omega)}{\int_{\omega_{min}}^{\omega_{max}} \sigma_{m}(\omega)} = \frac{f_{exc}}{f_m} \tag{S15}$$

where the integration limits are chosen such as to minimize overlap with adjacent bands. The total oscillator strengths for the monomer and the excited states (f_m and f_{exc}, respectively), if defined this way, will have a unit of [cm^2 eV].

The biggest sources of error are:

- Uncertainty of pump pulse intensity (20%)
- Uncertainty of density and local thickness (20%)
- Superposition of PB band with PA so that PB is underestimated (20%)
- Superposition with stimulated emission (SE) so that PB is overestimated (< 5% in conjugated polymers but up to 50% in rigid systems like phthalocyanines and carbon nanotubes)

The first two contributions dominate if L_{exc} values from different samples must be compared, while excited state localization due to exciton dissociation in a single experiment can be traced with higher precision.

c) Global and target analysis

Analysis of the pure D (donor) and A (acceptor). Femtosecond transient absorption (TA) spectroscopy is used to trace photophysics that occur on a time scale of femto to picoseconds. However, the spectral signatures of photoexcited states in TA spectra generally overlap, so matrix decomposition techniques need to be used to obtain the time-resolved populations of the various photoexcited states separately. The mathematics of the procedure has been described by van Stokkum *et al.*[S15] Here, we generalize to arbitrary photoexcitation dynamics.

We apply Beer-Lambert's Law,

$$A_c(t,\omega) = \sum_i c_i(t)\sigma_i(\omega) \tag{S16}$$

to find the calculated transient absorption $A_c(t,\omega)$ reproducing the measured transient absorption spectrum $A(t,\omega)$, which depends on time t and probe energy ω, by a superposition of states i with characteristic time-resolved concentration $c_i(t)$ and energy-dependent absorption cross-section $\sigma_i(\omega)$. Eq. S1 can be written in matrix form:

$$A_c = c \times \sigma \tag{S17}$$

In eq. S17, each column of the c matrix represents one complete concentration-time dependence of a state i, while each row of the σ matrix represents the full (time-invariant) spectrum of that state i. Of course, any linear combination σ' of the spectra in the σ matrix

$$\sigma' = s \times \sigma \tag{S18}$$

s being the spectral weight matrix, can also solve eq. S17, as can be seen by introducing S18 into S17:

$$A_c = c \times s^{-1} \times \sigma' \tag{S19}$$

and substituting $c \times s^{-1} \equiv c'$:

$$A_c = c' \times \sigma' \tag{S20}$$

Comparing S20 and S17 highlights the crux in global spectral modeling: There is an infinite number of combinations of c' and σ' that all reproduce the measured TA spectra perfectly. Our goal is to find the photophysical dynamics c and the photophysical spectra σ, not some linear combinations c' and σ'. Multiplying S17 by the inverse matrix of the spectra, σ^{-1}, we get

$$A_c\sigma^{-1} = c \tag{S21}$$

The interpretation of S21 is as follows: as there is only one inverse of the spectra, there is one and only one matrix c solving S21. Consequently, if the spectra of the photoexcited states are known, we are guaranteed to find the photophysical concentrations. Vice versa, if the concentrations are known, we are guaranteed to find the photophysical cross-sections.

In the present work, we find the spectra of the singlet excitons by performing TA spectroscopy on the pure donor (**D**) and acceptor (**A**) molecules. In Figure S8, we excited the pure **D** at 620 nm. The TA spectra in the near infrared spectral region are dominated by a single band at 1.03 eV. There is a shoulder at 1.2 eV which could be caused by additional states like triplets or charge states. If this were the case then these states should have different relaxation kinetics and therefore should cause a spectral evolution with the pump-probe delay time t. We can safely reject this scenario by perfect reproduction of the TA spectra at all probe wavelengths, delay times, and pump intensities with one set of parameters (namely k_a and k_{tr}) in a target model assuming only a single state (see Figure S9). The parameters k_a and k_{tr} are interpreted in the main manuscript as rate constants for exciton annihilation and trapping, allowing us to find the exciton diffusion constant and the density of traps.

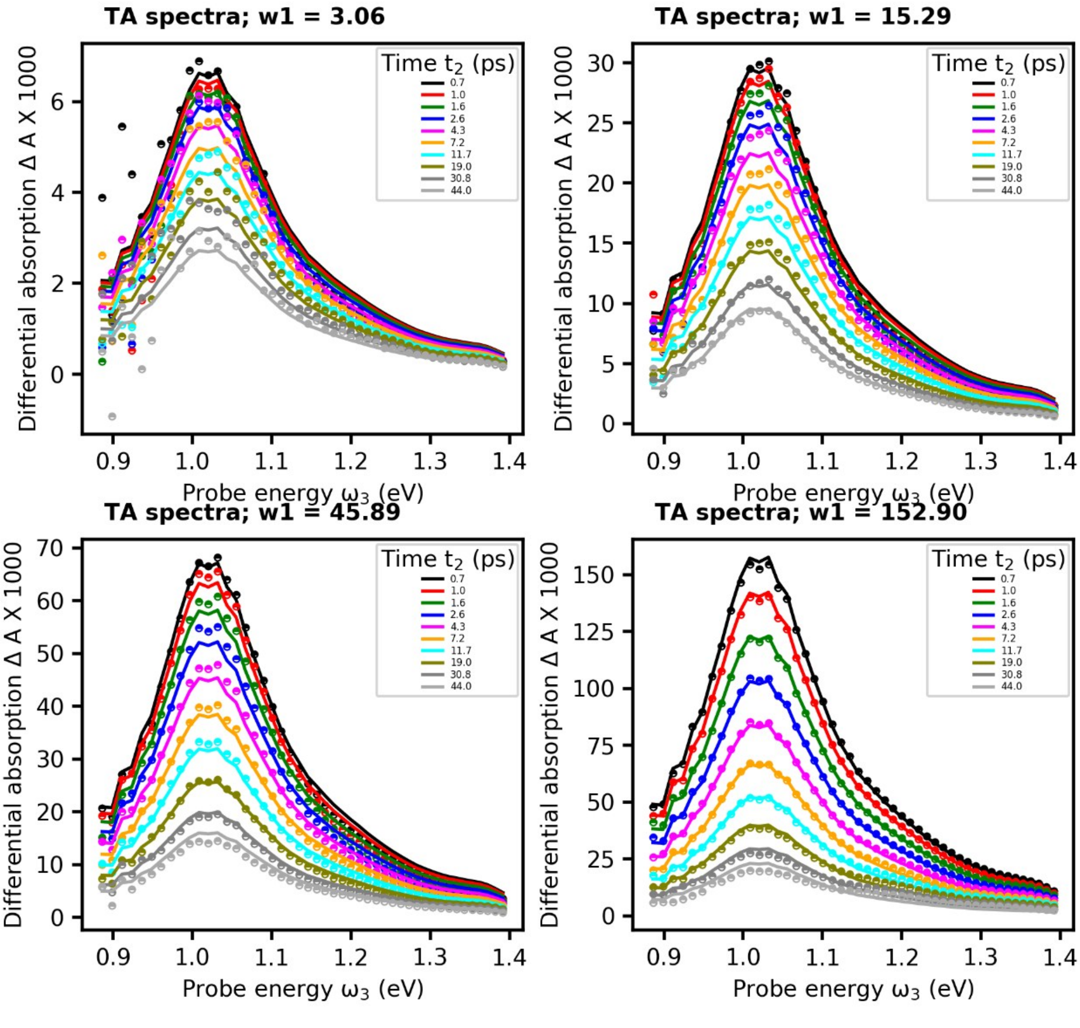

Figure S8: TA spectra of the donor pumped at 620 nm with four different pump energies, given as “w1” in µJ cm^{-2}. Symbols are experimental data points, lines of same color are global fits according to the target model depicted in Figure S9.

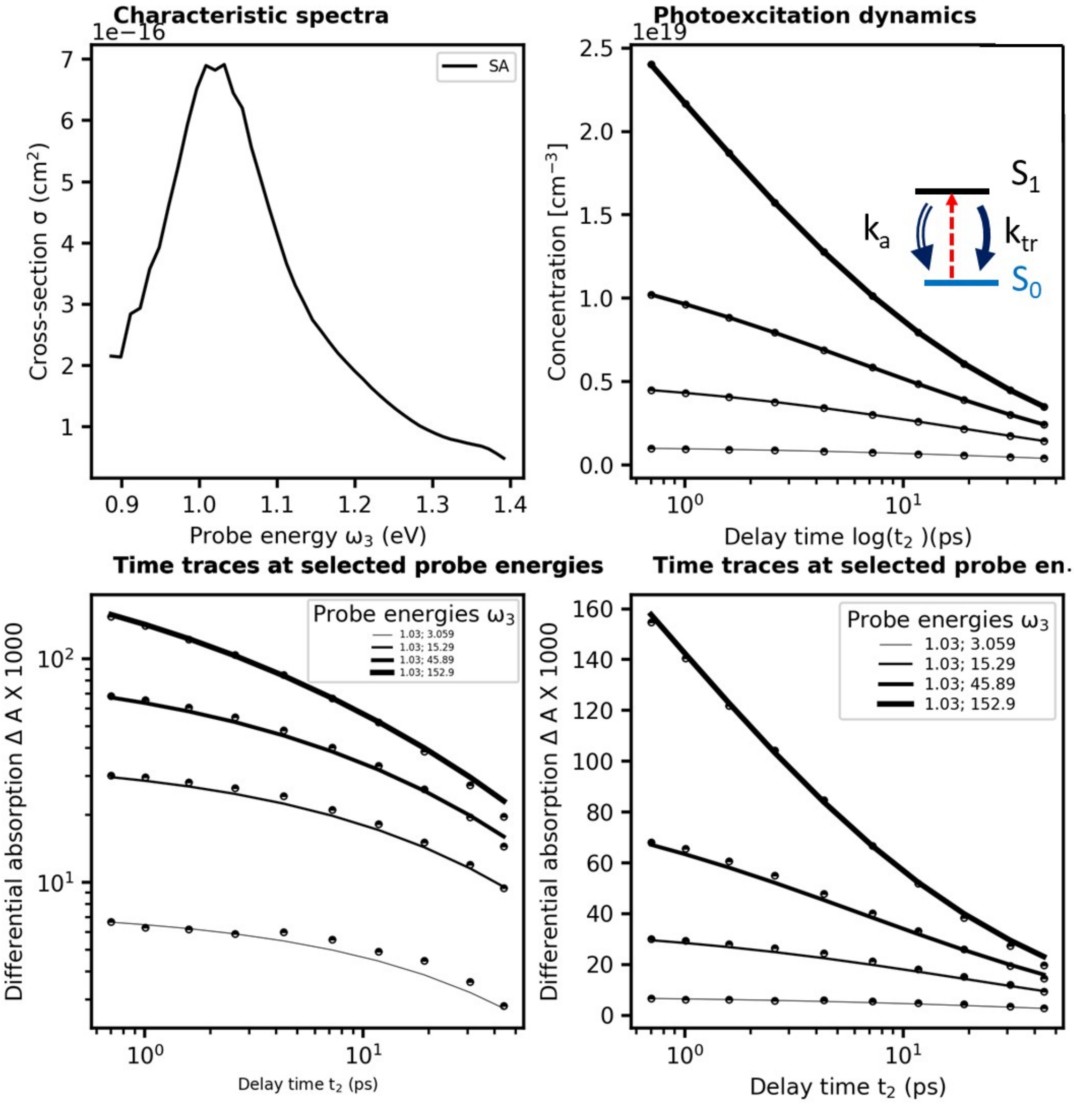

Figure S9: Result of target analysis of intensity dependent TA spectra in Figure S8. The target model is given in the right upper panel. An upward arrow indicates the excitation process, downward arrows indicate first order and second order relaxation processes (one-line and double-line arrows, respectively), here caused by diffusion-controlled exciton trapping and annihilation (rate constants k_{tr} and ka, respectively). The cross-sections and concentrations in the upper row correspond to σ and c in eq. S17.

In the same way, we obtain the characteristic spectrum and the relaxation constants from the pure **A** film excited at 510 nm, see Figure S10 and S11.

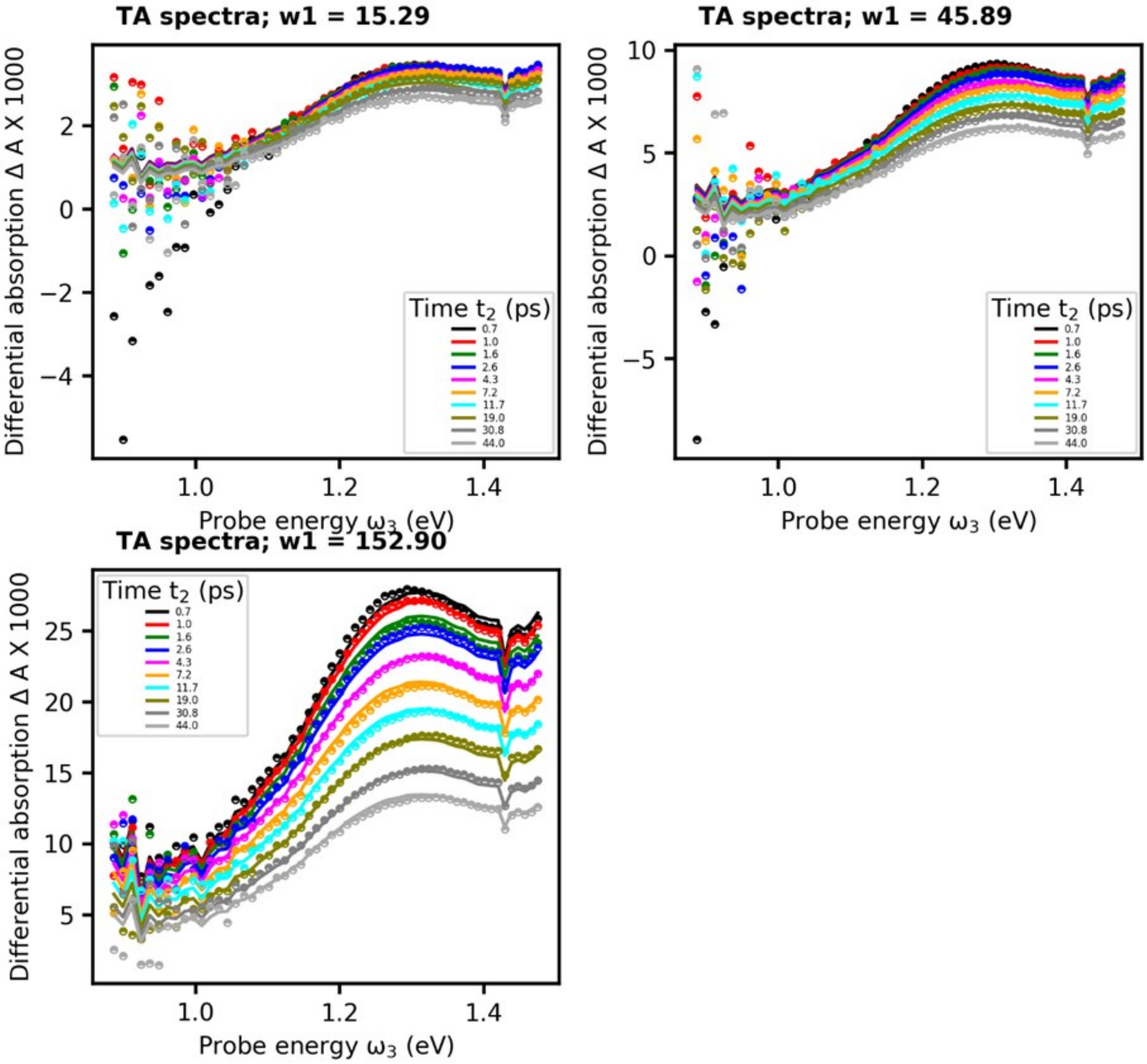

Figure S10: TA spectra of the acceptor pumped at 510 nm with three different pump energies, given as “w1” in μJ cm^{-2}. Symbols are experimental data points, lines of same color are global fits according to the target model depicted in Figure S11.

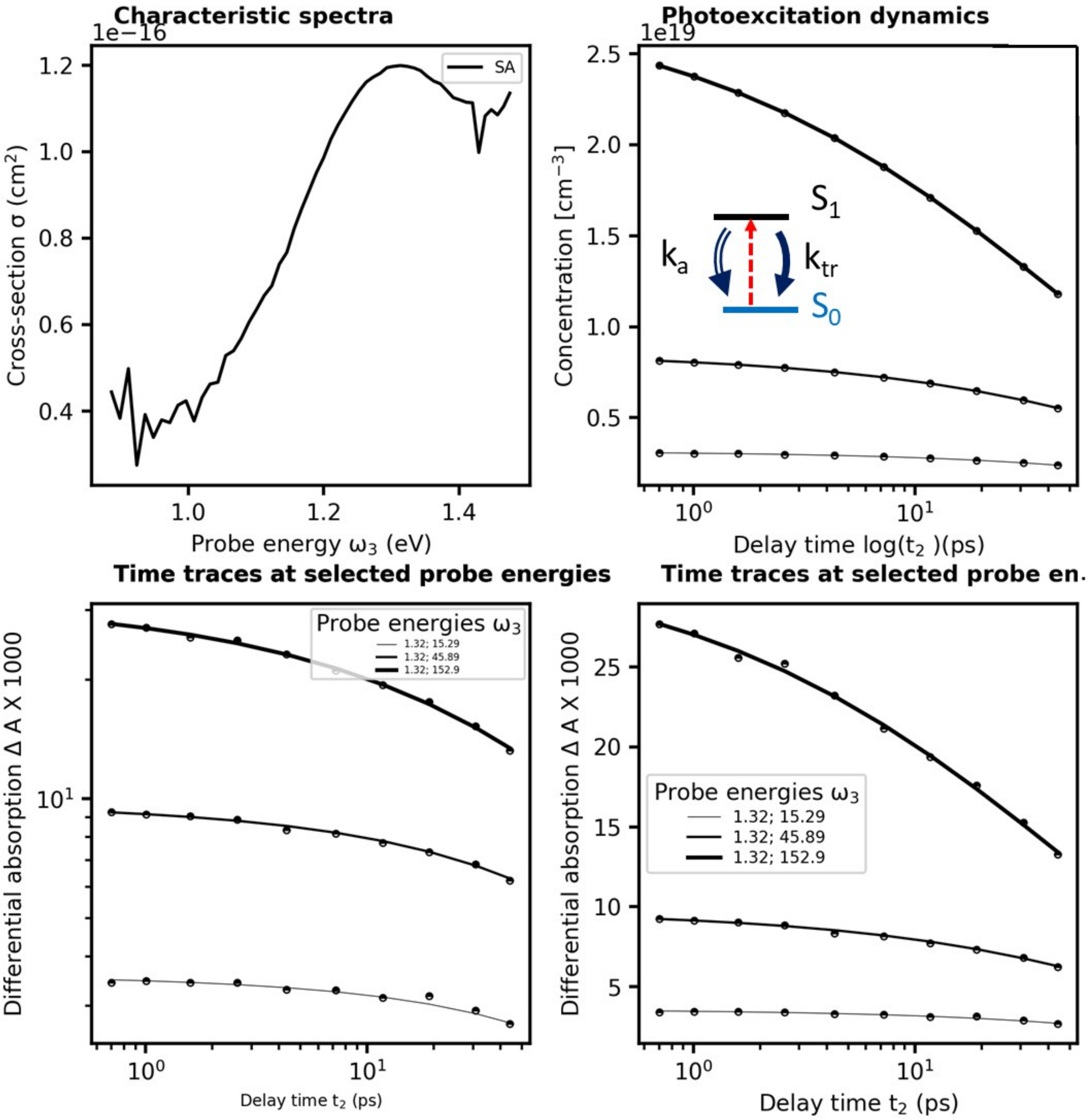

Figure S11: Result of target analysis of intensity dependent TA spectra in Figure S10. The target model is given in the right upper panel. An upward arrow indicates the excitation process, downward arrows indicate first order and second order relaxation processes (one-line and double-line arrows, respectively), here caused by diffusion-controlled exciton trapping and annihilation (rate constants k_{tr} and ka, respectively). The cross-sections and concentrations in the upper row correspond to σ and c in eq. S17.

Analysis of the blend sample. The information obtained in Figures. S8-11 is essential for the quantification of the elementary decay paths in the photovoltaic blends. We now have sufficient knowledge about the excited state absorption cross-sections of singlet states such that we can solve the rather complex target model for the blends, see upper right panels in Figures S13 and S15. As only two states are active in the overall relaxation process, precise knowledge of the spectral shape of the charge separated state is not necessary. Nonetheless, we verified that the excited state spectra we predict for the charge separated state coincide with nanosecond transient absorption spectra of the blends, thus assuring the long-lived nature of the species assigned to charge separated states.

In Figure S12, we show TA spectra of the as-deposited blend excited at 620 nm. We deploy the target model shown in Figure S13 and it fits perfectly. This confirms the overall layout of the target model, but not the value of the involved rate constants. To get these, we must exploit the information we got about the excited state spectra of the donor exciton. According to equation S20, we must adjust the matrix c' such that c'=c. Then according to eq. S21, σ'=σ. We accomplish this by tuning the rate constants of the target model until we find a satisfactory reproduction of the known σ of the singlet state. In our software realization (written in Python and based on open source packages such as numpy, scipy, matplotlib), this is done semi-automatically, by manually varying the charge transfer constant and optimizing the other parameters by nonlinear optimization. We find that only for a charge transfer rate of 1/25 ps, the resulting excited state spectra are acceptable. This notion is based on the following criteria:

- The absolute value of the cross-section of the singlet state is about 6e-16 cm^2, similar to the value obtained for the pure donor.
- The spectral shape of the donor singlet does not re-appear in the spectral shape of the charge separated state. If this were the case, it would demonstrate the presence of off-diagonal terms of the spectral weight matrix s in eq. S18. The obtained cross-sections would therefore be mixed states, not pure ones. According to eq. S21, if the cross-sections are mixed, the concentrations will also be mixed, and therefore wrong.
- The contribution of the *donor* photobleach (PB) region for both singlet and charge separated states is the same and agrees quantitatively with the cross-section for ground state absorption, compare with Figure S7. We have very little excitonic coupling, so we exclude dynamic exciton localization. Therefore, we know that our excited states, irrespective whether neutral or charged, occupy a single molecule. We can therefore require to find the value of $\sigma_{GSA} \approx 2 \cdot 10^{-16} cm^2$ that we obtain from Figure S7, for both singlets and charged states. This is exactly the case.

- The contribution of the *acceptor* PB increases due to the charge separation process because we resonantly pump the donor excitons.

In the same way, we analyze the TA spectra of the annealed blend, see Figures S14 and 15. The fits are perfect, so the layout of the target model is good. Only for a charge transfer rate of 1/100 ps, we are able to minimize the presence of the sharp and easily visible donor singlet state in the cross-section spectrum for the charge separate state. At 1.03 eV, the maximum of the **D** singlet state, we find only an oscillatory behavior, which might point to a first derivative component in the deactivation of the **D** singlet state, e.g. by spectral relaxation.

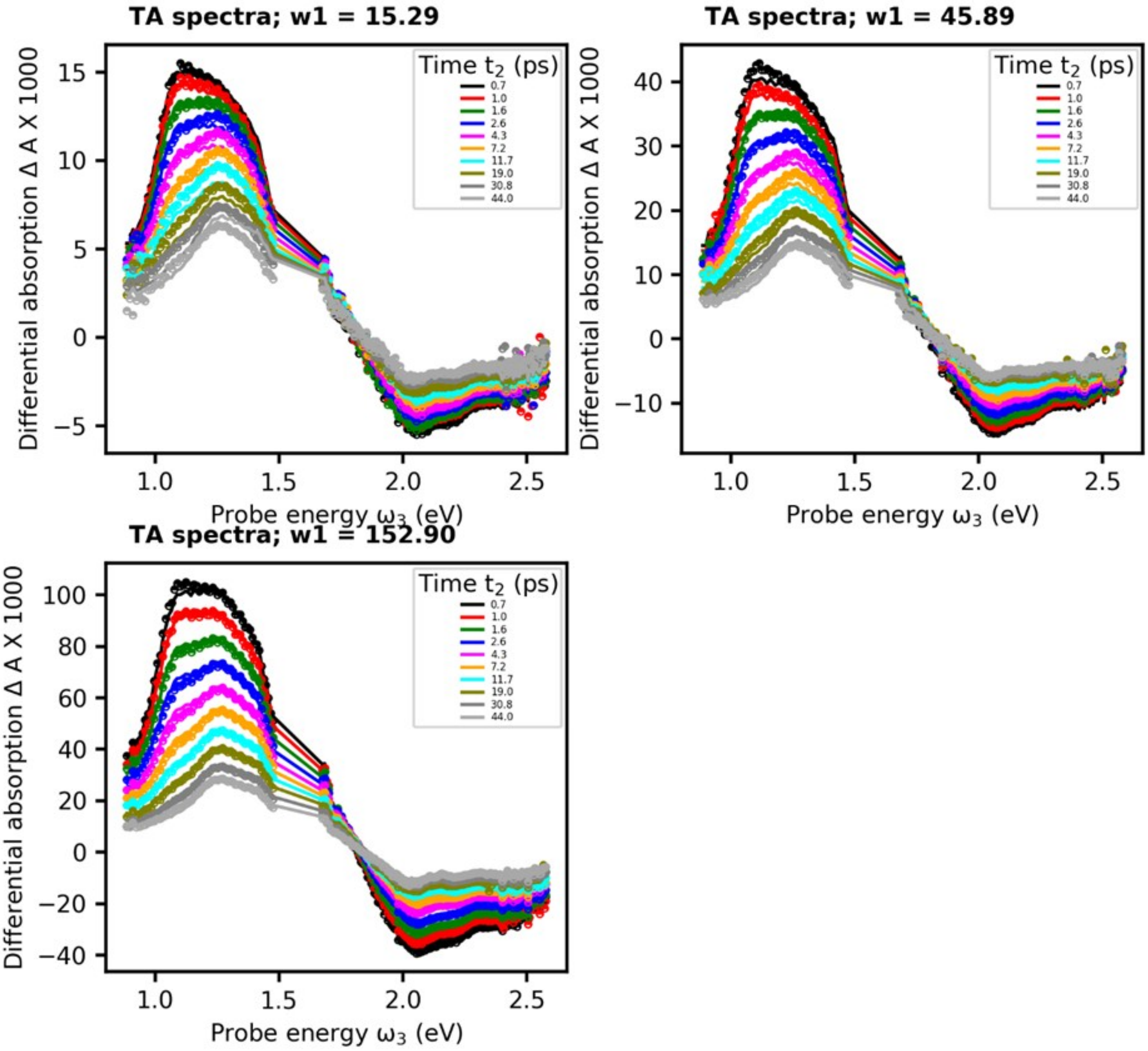

Figure S12: TA spectra of the as-deposited blend pumped at 620 nm with three different pump energies, given as “w1” in µJ cm^{-2}. Symbols are experimental data points, lines of same color are global fits according to the target model depicted in Figure S13.

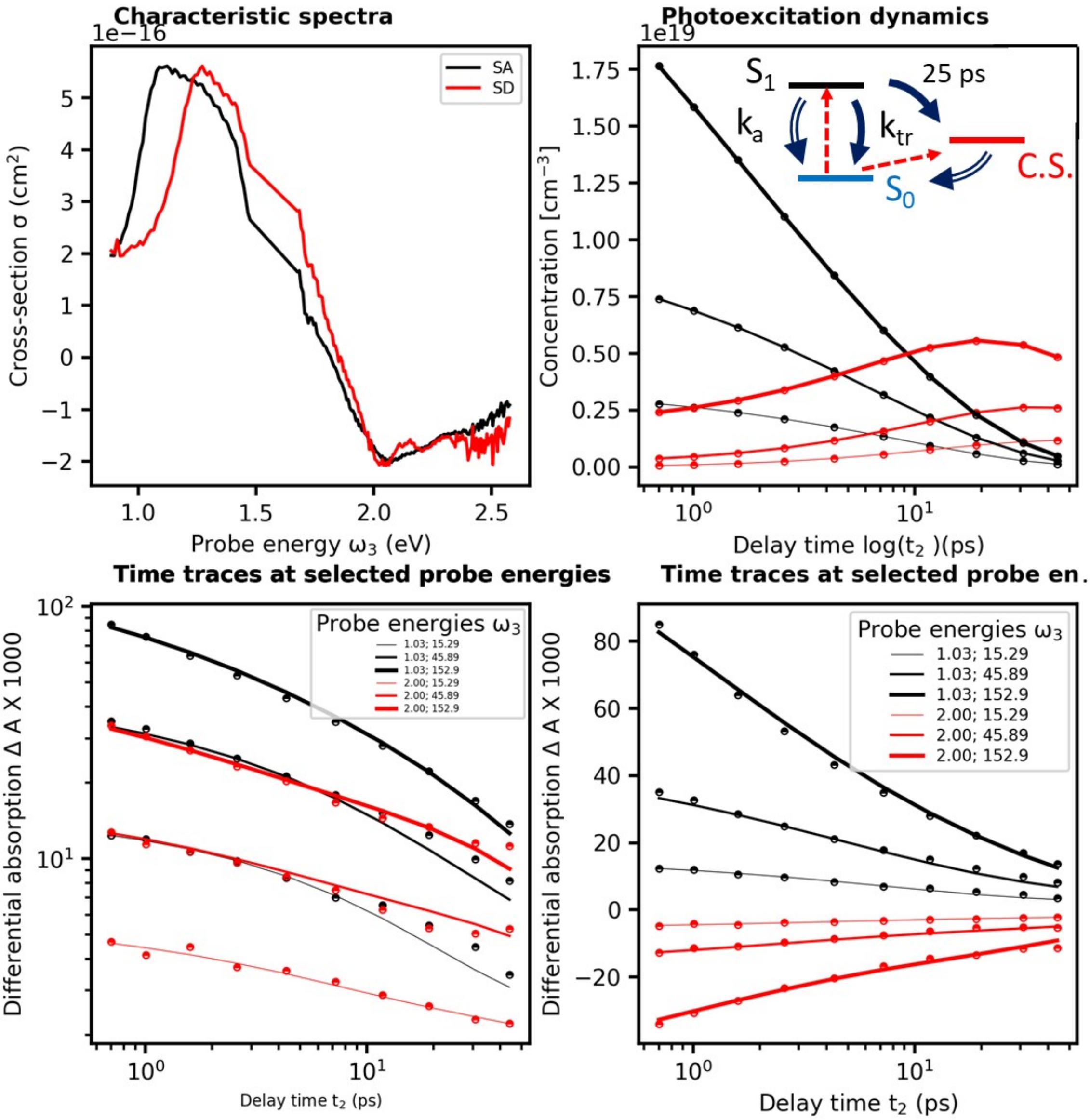

Figure S13: Result of target analysis of intensity dependent TA spectra in Figure S12. The target model is given in the right upper panel. Photoexcited states appear in same color as the corresponding cross-sections and concentrations in the upper row of the figure. Upward arrows indicate the excitation process, downward arrows indicate first order and second order relaxation processes (one-line and double-line arrows, respectively).

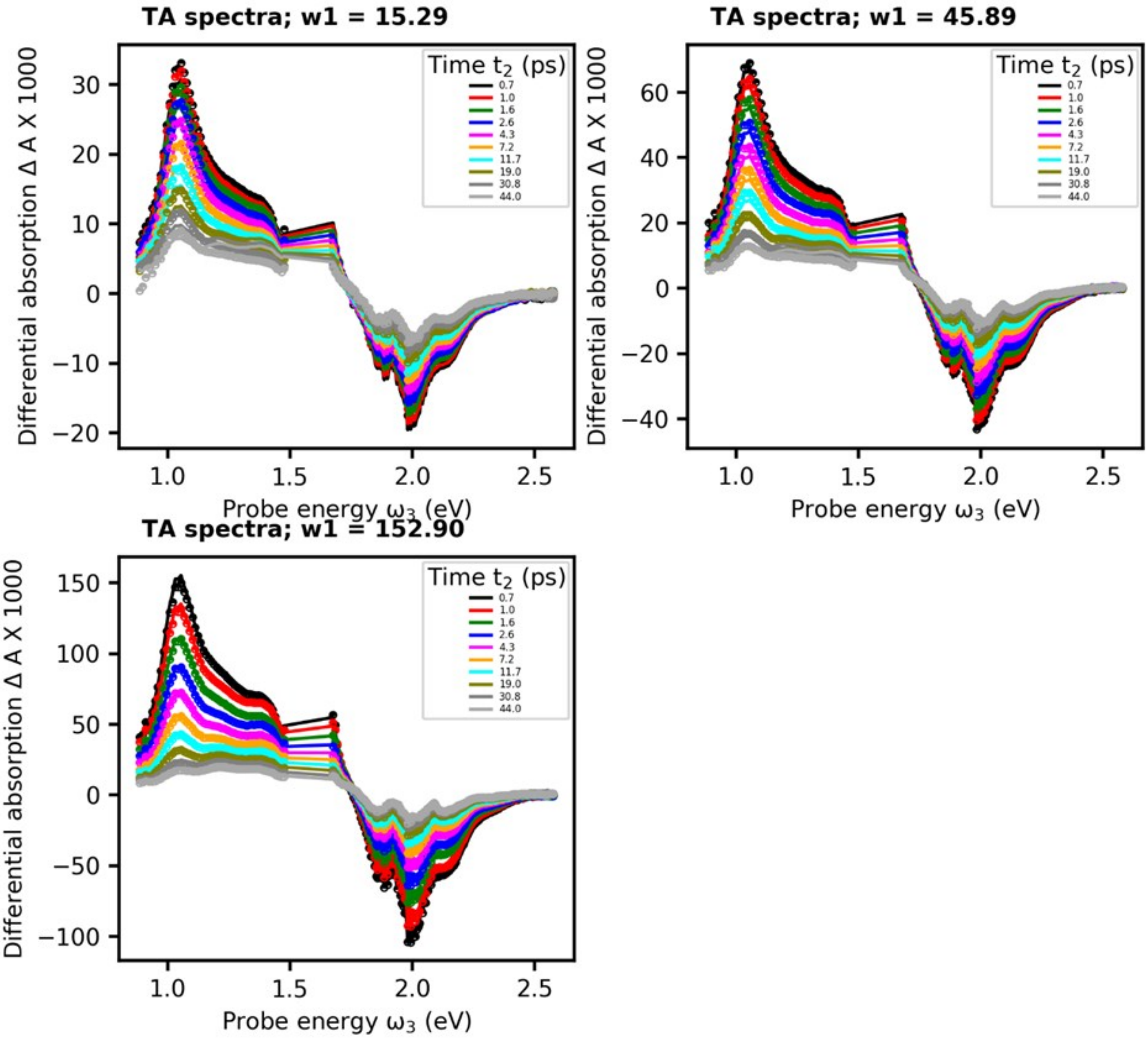

Figure S14: TA spectra of the annealed blend pumped at 620 nm with three different pump energies, given as “w1” in µJ cm^{-2}. Symbols are experimental data points, lines of same color are global fits according to the target model depicted in Figure S15.

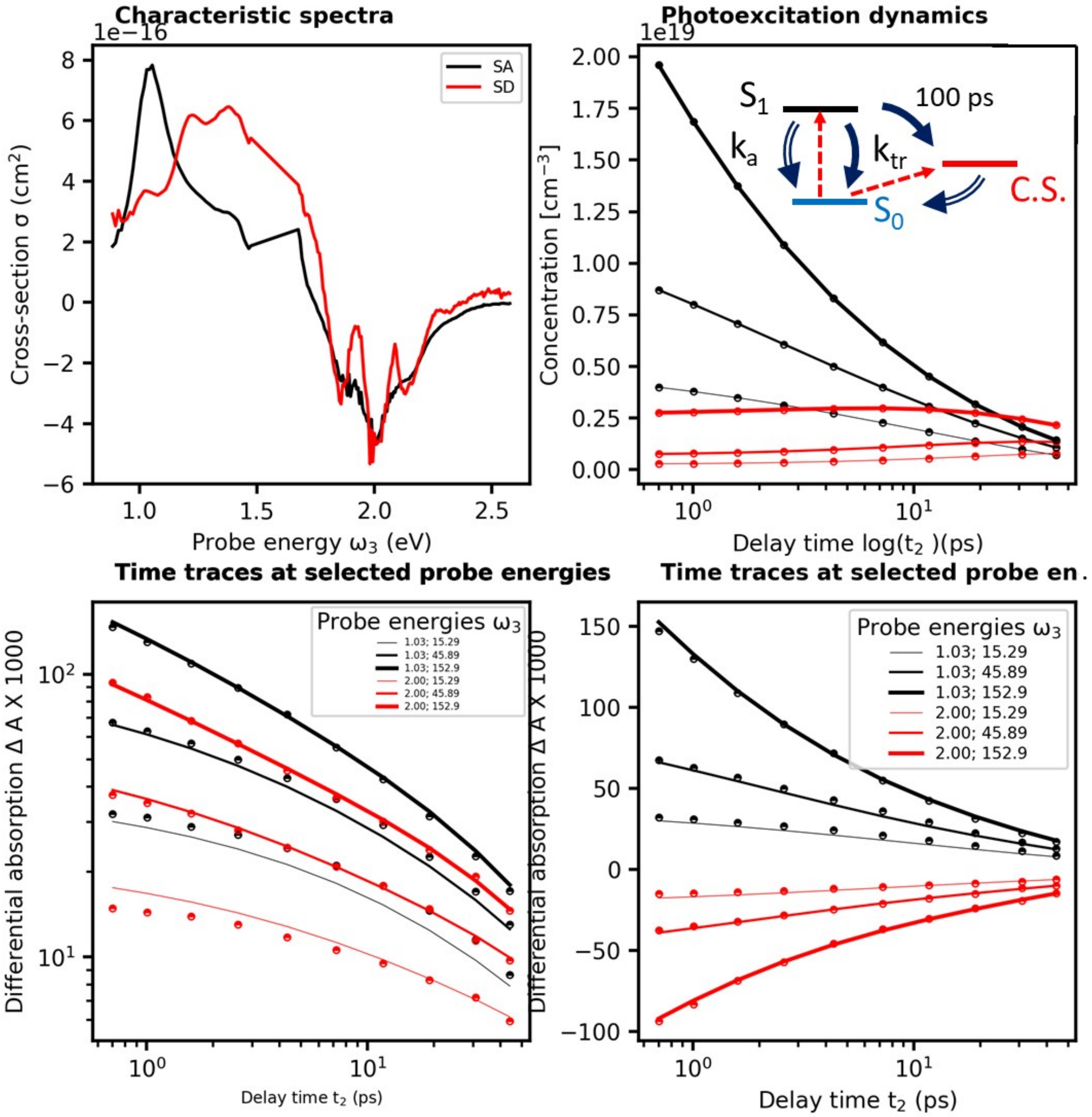

Figure S15: Result of target analysis of intensity dependent TA spectra in Figure S14. The target model is given in the right upper panel. Photoexcited states appear in same color as the corresponding cross-sections and concentrations in the upper row of the figure. Upward arrows indicate the excitation process, downward arrows indicate first order and second order relaxation processes (one-line and double-line arrows, respectively).

F Exciton Diffusion

We have modeled singlet exciton dynamics by assuming diffusion-controlled exciton quenching at indestructible quenching sites at a concentration c_Q, assumed homogeneous, in parallel with diffusion-enhanced exciton annihilation by a Foerster resonance energy transfer mechanism with typical annihilation distance R_a.

For both processes, we assume the same exciton diffusion constant D_{exc} so that the rate equation becomes:[S16]

$$\frac{dS}{dt} = -k_q^0(t) \cdot S - \left(k_q^\infty + k_F + k_{nr} + k_{ct}\right) \cdot S - \left(k_a^0(t) + k_a^\infty\right) \cdot S^2 \tag{S22}$$

Herein, in the case of three-dimensional diffusion, $k_q^0(t) = 4\pi \cdot R_q^2 \cdot D_{exc} \cdot c_Q / \sqrt{2\pi D_{exc} t}$, $k_q^\infty = 4\pi \cdot R_q \cdot D_{exc} \cdot c_Q$, $k_a^0(t) = \frac{2}{3}\pi^{3/2} R_a^3 \tau_F^{-1/2}$, and $k_a^\infty = 4\pi \cdot 0.676 \cdot D_{exc}{}^{3/4} \cdot R_0^{3/2} \cdot \tau_F^{-1/4}$, while in the case of predominantly one-dimensional diffusion, $\left(k_q^\infty = k_a^\infty\right) \approx 0$, $k_q^0(t) = 4\pi \cdot D_{exc} \cdot R_q^2 \cdot c_Q / \sqrt{\pi D_{exc} t}$ and $k_a^0(t) = 2\pi \cdot R_q^2 \cdot D_{exc} \cdot c_Q / \sqrt{\pi D_{exc} t}$. The parameter k_{ct} is the exciton dissociation (charge transfer) constant at the **D-A** interface which we set zero for the pure **A** and **D** films. Assuming electron transfer as the quenching mechanism, we can set the reaction radius to the nearest neighbor distance of R_q=1 nm. [S17]

G Calculation of the Free Carrier Yield in a Bulk Heterojunction Solar Cell

The overall chain of photovoltaic elementary processes is summarized in Scheme S2.

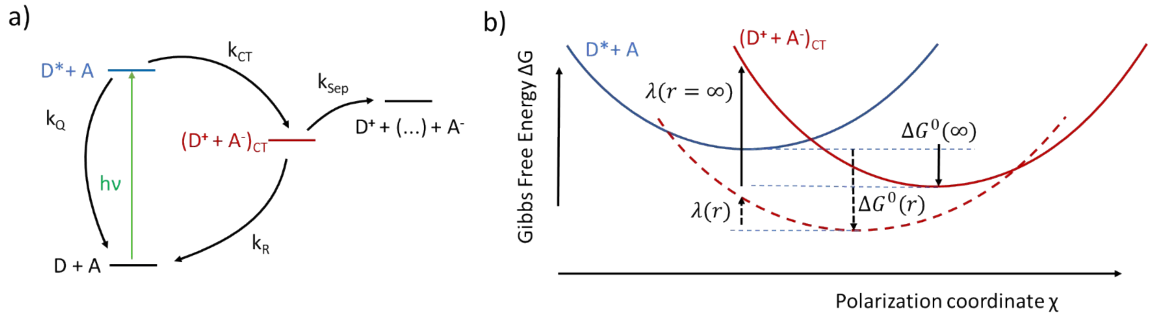

Scheme S2: a) Elementary processes for free carrier generation in a bulk heterojunction solar cell, b) Gibbs free energy (ΔG) surfaces as function of the polarization coordinate χ, showing the dependence of the driving force ΔG^0 and the reorganization energy λ on the center-to center distance r of the donor (**D**) and acceptor (**A**) excess charge densities, for the electronic states involved in the calculation of k_{CT}. Similar representations can be given for the calculation of k_R and k_{Sep}.

According to Scheme S2a, the yield of free carriers is given by

$$\phi_{fc} = \phi_{CT} \cdot \phi_{Sep} = \frac{k_{CT}}{\left(k_{CT} + k_Q\right)} \cdot \frac{k_{Sep}}{\left(k_{sep} + k_R\right)}, \tag{S23}$$

where ϕ_{CT} and ϕ_{sep} are the yields for charge transfer and charge separation, respectively, and k_{CT}, k_Q, k_{Sep}, and k_R are the rates for charge transfer, exciton quenching, charge separation and charge recombination, respectively. By a target analysis, we have found an experimental value for k_Q and a lower limit for k_{CT} (since in the annealed sample, charge transfer is diffusion controlled). The three relevant charge transfer processes $Y \epsilon \{CT, Sep, R\}$ can be described by semiclassical Marcus theory:

$$k_Y = \sqrt{\frac{\pi}{\hbar^2 \lambda_s(r) k_B T}} |V(r,p)|^2 \sum_{n=1}^{\infty} \frac{e^{-S} S^n}{n!} exp\left[\frac{-\left(nE_v + \lambda_s(r) + \Delta G_Y^0(r)\right)^2}{4\lambda_s(r) k_B T}\right] \tag{S24}$$

where the Huang-Rhys factor is given by $S = \lambda_v / E_v$, λ_v being the internal reorganization energy and E_v the vibrational energy of an effective mode. The external reorganization energy is given by $\lambda_s(r)$, where r is the center-to center distance of the oxidized donor (**D**) and reduced acceptor (**A**) excess charge densities, υ is the vibrational quantum number, V is the coupling between **D** and **A**, k_B is Boltzmann's constant, and $\Delta G_Y^0(r)$ is the Gibbs free energy change ("driving force") for charge transfer process Y. Ignoring entropy contributions to the driving force, we can express ΔG_Y^0 as the difference of the minima of the potential energy surfaces of the final and initial states for process Y, $E_f(\chi)$ and $E_i(\chi)$, respectively, both depending on the polarization coordinate χ (see Scheme S2b):

$$\Delta G_0^Y = \min\left(E_f^Y(\chi)\right) - min\left(E_i^Y(\chi)\right) \tag{S25}$$

Since the quantities on the right side of eq. S25 are not directly accessible, we need to introduce a series of intermediate steps that are accessible either experimentally or by quantum chemical calculations. Weller has derived a simple formula for the energy of the final state, starting from cyclovoltammetric measurements of the donor first oxidation and acceptor first reduction potentials and considering the dependence of the solvation enthalpies of the final state in solvents of different dielectric constant. [S18] However, in their derivation, they did not consider the solvation enthalpy of the neutral initial state. By writing down reversible pathways for solvation of ground, excited and charged states, optical excitation and charge transfer, one can show that Weller's equation remains valid if one assumed that the solvation enthalpy of ground states does not depend on the dielectric constant. The correct equation for the driving force for charge transfer, explicitly considering solvation of neutral species, is given by:

$$\Delta G_0^{CT} = - E_{opt} + E_{ox}^{D} - E_{red}^{A} + k\left(- \frac{1}{2\varepsilon_{ref} r_d} - \frac{1}{2\varepsilon_{ref} r_a} + \frac{1}{2\varepsilon_{inf}^{ref} r_d} + \frac{1}{2\varepsilon_{inf}^{ref} r_a} - \frac{1}{2\varepsilon_{inf} r_d} - \frac{}{2\varepsilon_{i}} \right. \quad \text{(S26)}$$

with $k = q^2/(4\pi\varepsilon_0)$, E_{opt} = 1.77 eV as the optical bandgap of the donor, $E_{ox}^{D} = qP_{ox}^{D} = 5.12\ eV$ and $E_{red}^{A} = qP_{red}^{A} = 3.66\ eV$ are the first oxidation and first reduction potentials, respectively, of the donor and acceptor, respectively, times the unit charge q to obtain energy units and measured by cyclovoltammetry in dichloromethane, r_d and r_a are the radii of the cavities (assumed spherical) occupied by the donor and acceptor, respectively, obtained by calculating the volume occupied by the molecules from their molecular mass and assuming a density of $\rho_{film} = 1.3\ g/cm^3$, $\varepsilon_r = 4.0$ is the relative dielectric constant, assumed isotropic, of the **D:A** blend, $\varepsilon_{ref} = 8.93$ is the relative dielectric constant of dichloromethane, $\varepsilon_{inf} = \varepsilon_{inf}^{ref} = 3.5$ is the optical relative dielectric constant of both dichloromethane and the **D:A** blend. The coulomb energy E_c is given by

$$\Delta E_C(r) = \sum_{d \in D^+, a \in A^-} \frac{q_d q_a}{4\pi\varepsilon_0\varepsilon_r r} \quad \text{(S27)}$$

where the overall excess charge density of **D+** and **A-** is represented as partial point charges q_a and q_d on acceptor and donor atoms, respectively, as can be obtained by a Mulliken population analysis. Using these values, we can draw the potential energy parabola for the ground state, the excited state and the charge separated state, see Fig. S16. It is clearly displayed that for the parameters chosen, charge transfer proceeds virtually without activation energy thus justifying the relative independence of the charge transfer rate k_{ct} of the **D-A** distance r (see Fig. 5a in main text), defined as the distance between the centers of gravity of the donor and acceptor excess charge distributions. It is further displayed that charge recombination proceeds far in the Marcus inverted region, thus justifying the increase of k_{CR} with decreasing distance, see Fig. 5b in main text. Further parameters for the calculation of Fig.6 in main manuscript were: $\lambda_v = 0.12\ eV$, $a_0 = 0.5$ nm (hopping distance) to calculate a hopping rate $k_{hop} = \frac{1}{t_{hop}} = D/a_0^2$, being the inverse of the hopping time, where the diffusion constant is calculated via the Einstein relation $D = \mu k_B T$, where $\mu = 10^{-4} cm^2/Vs$ is the effective charge mobility taken from reference [S19], $k_B = 8.617 \cdot 10^{-5} eV/K$ is Boltzmann's constant, and T = 293 K is the temperature. As a crude estimate for the charge separation rate k_{sep} in Scheme S2a and eq. S23, we use the rate of activated transfer according to $k_{sep}(r) \approx k_{hop} \exp\left[-\left(\Delta E_g(r + a_0) - \Delta E_g(r)\right)/k_B T\right]$, that is, the hopping rate at a **D-A** distance r towards the nearest more distant neighbor.

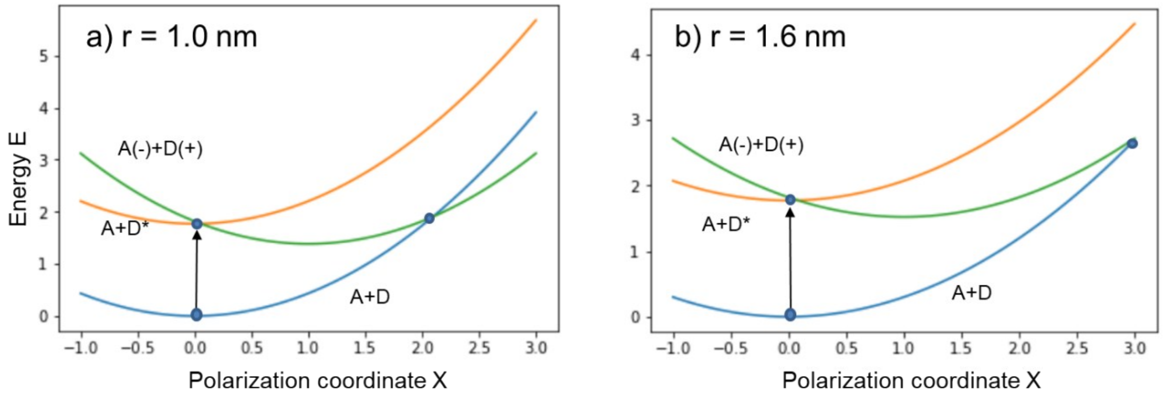

Figure S16: Potential energy parabola, as function of the polarization coordinate X, for the ground state, the donor singlet excited state, and the charge separated state (blue, orange, green parabola, respectively), at two different **D-A** distances r (panels a and b).

References

[S1] M. Reichenberger, J. A. Love, A. Rudnick, S. Bagnich, F. Panzer, A. Stradomska, G. C. Bazan, T.-Q. Nguyen, A. Köhler, *J. Chem. Phys.*, 2016, **144**, 074904.

[S2] J. Gierschner, H.-G. Mack, L. Lüer, D. Oelkrug, *J. Chem. Phys.*, 2002, **116**, 8596-8609.

[S3] B. Milián-Medina, S. Varghese, R. Ragni, H. Boerner, E. Ortí, G. M. Farinola, and J. Gierschner, *J. Chem. Phys.*, 2011, **135**, 124509.

[S4] J. Shi, S.-J. Yoon, L. Viani, B. Milián-Medina, S. Y. Park, J. Gierschner, *Adv. Opt. Mater.*, 2017, **5**, accepted.

[S5] M. J. Frisch et al, Gaussian 09 - Revision D.01, Gaussian, Inc., Wallingford CT, 2009.

[S6] J. A. Love, C. M. Proctor, J. Liu, C. J. Takacs, A. Sharenko, T. S. van der Poll, A. J. Heeger, G. C. Bazan, T.-Q. Nguyen, *Adv. Funct. Mater.*, 2013, **23**, 5019-5026.

[S7] A. Drechsler, M. A. Lieb, C. Debus, A. J. Meixner, G. Tarrach, *Opt. Express*, 2001, **9**, 637-644.

[S8] J. Rogalski, K. Braun, A. Horneber, M. van den Berg, J. Uihlein, H. Peisert, T. Chassé, A. J. Meixner, D. Zhang, *Vibr. Spectroscop.*, 2017, **91**, 128-135.

[S9] X. Wang, D. Zhang, K. Braun, H.-J. Egelhaaf, C. J. Brabec, A. J. Meixner, *Adv. Funct. Mater.*, 2010, **20**, 492–499.

[S10] X. Wang, H. Azimi, H.-G. Mack, M. Morana, H.-J. Egelhaaf, A. J. Meixner, D. Zhang, *Small*, 2011, **7**, 2793–2800.

[S11] X. Wang, H.-J. Egelhaaf, H.-G. Mack, H. Azimi, C. J. Brabec, A. J. Meixner, D. Zhang, *Adv. Energy Mater.*, 2014, 1400497.

[S12] A. Horneber, K. Braun, J. Rogalski, P. Leiderer, A. J. Meixner, D. Zhang, *Phys.Chem.Chem.Phys.*, 2015, **17**, 21288-21293.

[S13] S. Schmitt-Rink, D. S. Chemla, D. A. B. Miller, *Phys. Rev. B.*, 1985, **32**, 6601-6609.

[S14] L. Lüer, S. Hoseinkhani, D. Polli, J. Crochet, T. Hertel, G. Lanzani, *Nature Phys.,*2009, **5**, 54–58.

[S15] I. H. M. Van Stokkum, D. S. Larsen, R. van Grondelle, *Biochimica et Biophysica Acta*, 2004, **1658**, 82–104.

[S16] U. M. Goesele, *Prog. Reaction Kinetics*, 1984, **13**, 63-161.

[S17] J. D. A. Lin, O. V. Mikhnenko, J. Chen, Z. Masri, A. Ruseckas, A. Mikhailovsky, R. P. Raab, J. Liu,. P. W. M. Blom, M. A. Loi, C. J. Garcia-Cervera, I. D. Samuel, T-Q. Nguyen, *Mater. Horiz.*, 2014, **1**, 280-285.

[S18] A. Weller, *J. Phys. Chem.*, 1982, **133**, 93-98.

[S19] O. K. Kwon, J.-H. Park, S. K. Park, S. Y. Park, *Adv. Energy Mater.*, 2015, **5**, 1400929.